Pushing the High-Energy Limit of Plasmonics

Francesco Bisio,[†,*] Remo Proietti Zaccaria,[‡] Riccardo Moroni,[†] Giulia Maidecchi,[§] Alessandro Alabastri,[‡] Grazia Gonella,[⊥] Angelo Giglia,[∥] Laura Andolfi,[∥] Stefano Nannarone,[∥] Lorenzo Mattera,[§] and Maurizio Canepa[§]

[†]CNR-SPIN, C.so Perrone 24, I-16152 Genova, Italy, [‡]Istituto Italiano di Tecnologia, Via Morego 30, I-16163 Genova, Italy, [§]Dipartimento di Fisica, Università di Genova and CNISM, Sede Consorziata di Genova, via Dodecaneso 33, I-16146 Genova, Italy, [⊥]Department of Chemistry, Temple University, Philadelphia, Pennsylvania 19122, United States, and [∥]CNR-Istituto Officina Materiali, I-34149 Trieste, Italy

ABSTRACT The localized surface plasmon resonance of metal nanoparticles allows confining the eletromagnetic field in nanosized volumes, creating high-field "hot spots", most useful for enhanced nonlinear optical spectroscopies. The commonly employed metals, Au and Ag, yield plasmon resonances only spanning the visible/near-infrared range. Stretching upward, the useful energy range of plasmonics requires exploiting different materials. Deep-ultraviolet plasmon resonances happen to be achievable with one of the cheapest and most abundant materials available: aluminum indeed holds the promise of a broadly tunable plasmonic response, theoretically extending far into the deep-ultraviolet. Complex nanofabrication and the unavoidable Al oxidation have so far prevented the achievement of this ultimate high-energy response. A nanofabrication technique producing purely metallic Al nanoparticles has at last allowed to overcome these limits, pushing the plasmon resonance to 6.8 eV photon energy (≈180 nm) and thus significantly broadening the spectral range of plasmonics' numerous applications.

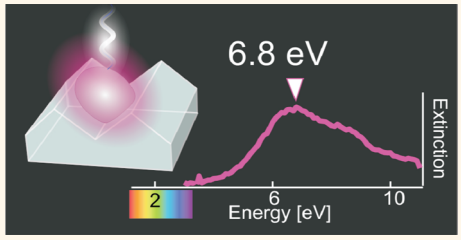

KEYWORDS: plasmonics · aluminum · ultraviolet · nanoparticle · self-organization

Aluminum is one of the most promising materials for the future of plasmonics, and the one that is attracting an ever growing attention.[1−20] The main factors behind the rise of aluminum are the large sensitivity of its localized-surface-plasmon (LSP) frequency to relatively small variations of nanoparticle (NP) size,[5,9] the broad plasmonic spectral range attainable,[3,5] the compatibility with CMOS technology,[21] and last but not least, its great abundance on the Earth's crust.

In the small-particle limit, the LSP resonances of Al may theoretically reach up to the deep ultraviolet (DUV) electromagnetic (EM) range, a feature unparalleled by the more traditional plasmonic metals Au and Ag.[22,23] Several factors have however stood in the way of reaching this theoretical value. When pushing the high-energy limits of Al plasmonics, indeed, the strong dependence of the LSP on the NP size turns into a disadvantage, as NP radii above 10 nm already suffice to significantly redshift its plasmon resonance.[9] Additionally, aluminum, unlike Au or Ag, is subjected to the quick formation of a few-nanometers-thick oxide layer upon exposure to atmosphere,[24] that redshifts the LSP with respect to the pure-metal case.[9]

The objective difficulty in fabricating and characterizing Al nanostructures in their purely metallic state has so far restricted any research activity on oxide-free Al plasmonics to theoretical calculations.[9,22,25] Supporting these theoretical predictions with the experimental observation of the plasmonic response of metallic Al NPs would provide a benchmark for testing the theory, understanding the dielectric properties of the Al free electrons under confinement and, more fundamentally, exploring the actually attainable high-energy limits of plasmonics.

In this work, we report the observation of the LSP resonances of Al nanoparticles, arranged in two-dimensional (2D), high-density arrays on the nanopatterned surface of insulating LiF(110) single crystals. The systems were fabricated and characterized under strict ultra-high vacuum (UHV) conditions, without exposing the samples to atmosphere between fabrication and measurement

* Address correspondence to francesco.bisio@spin.cnr.it.

Received for review June 4, 2014 and accepted September 2, 2014.

Published online September 02, 2014
10.1021/nn503035b

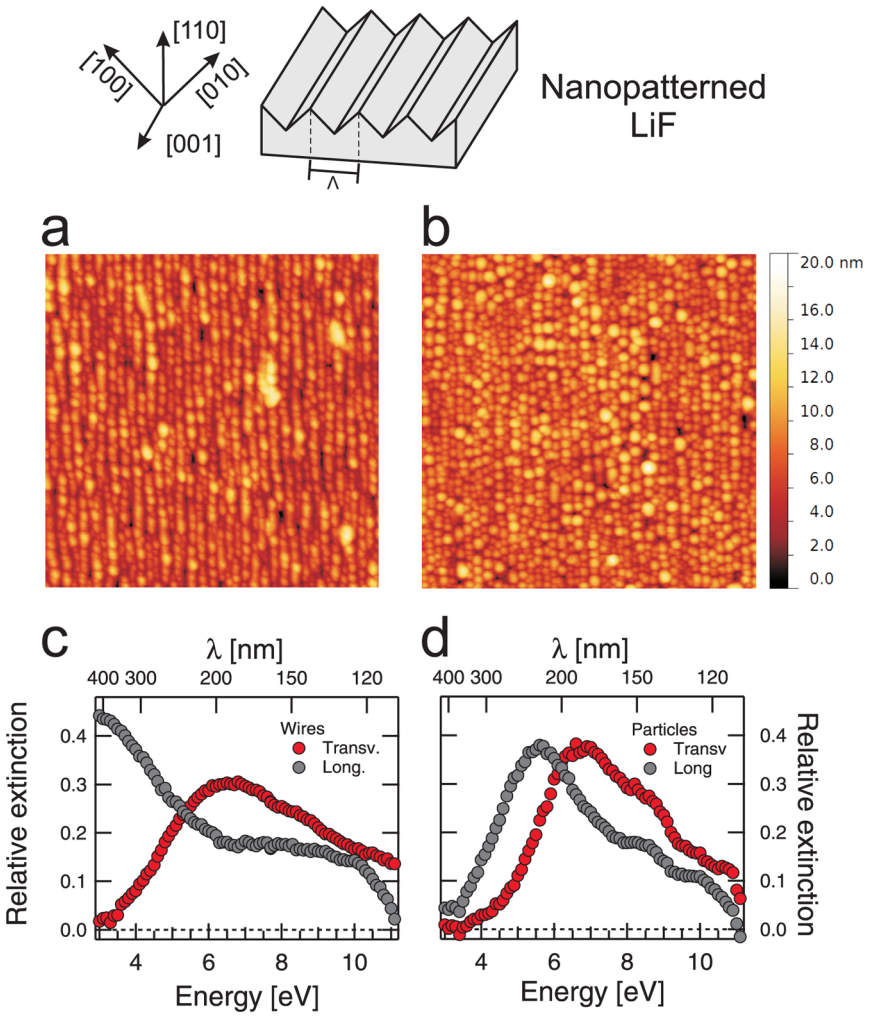

Figure 1. Morphology and plasmonic response of NW and NP arrays. (Top) Schematic drawing of a nanopatterned LiF(110) surface. (a and b) AFM image of Al nanowires and nanoparticle arrays. The images have been recorded *ex situ* on sacrificial samples. The image size is 1 × 1 μm^2. (c) Extinction spectrum of nanowires in the *L* (gray markers) and *T* (red markers) geometry. (d) Extinction spectrum of nanoparticles in the *L* (gray markers) and *T* (red markers) geometry.

thus preventing any significant oxidation of the Al surface. The Al NPs exhibit a strikingly high LSP energy, with a main dipolar resonance at 6.8 eV (≈180 nm), far beyond any currently reported value. The plasmon excitation is very broad toward the high-energy side, remaining sizable up to 9−10 eV photon energy, due to multipolar resonances arising from the combined effect of single-particle characteristics and mutual electromagnetic coupling. The availability of purely metallic particles uniquely allowed to directly monitor the oxidation effects on the LSP, from the very start of the phenomenon. Comparing data with theoretical calculations not only allowed to rationalize the optical response of the NPs, but also hinted at possible shape evolutions of the metallic core during oxidation.

RESULTS AND DISCUSSION

The samples consisted of 2D arrays of metal nanowires (NW) or NPs, supported on ridge-valley nanopatterned LiF(110) surfaces (Figure 1, top).[2,26,27] NWs were fabricated depositing 2.5 nm of equivalent thickness of Al, at grazing incidence, on the nanopatterned surface, while NPs were realized by annealing the NWs. All samples were fabricated in UHV, and maintained in UHV all the time between the fabrication and their measurement, but a few sacrificial samples were extracted from the experimental chamber in correspondence of various stages of sample preparation, in order to be characterized *ex situ* by AFM, thus providing a snapshot of the NW and NP array morphology.

In Figure 1a,b, we report two representative AFM images of Al NWs and NPs, respectively (the image size is 1 × 1 μm^2, the height color scale is the same for both images). The images have been acquired *ex situ* on two distinct sacrificial samples shortly after their fabrication. Although the unavoidable oxidation of these samples induces a partial swelling of the nanostructures, the images are fully representative of the NW and NP array morphology. A large number of small, densely packed clusters, aligned along the direction of the LiF

nanoridges, is clearly visible in both images. In the as-deposited case (nanowires), the deposition induced the formation of Al wires, whose rough, mound-like surface most likely arises because of Stranski-Krastanov growth. The mounds' edges clearly become sharper and better defined in the annealed case, suggesting a morphological evolution of the system that, according to our previous work,[2,27] can be safely assigned to the thermal dewetting of the NWs and the consequent formation of disconnected NPs aligned along the LiF nanoridges. The NP density deduced by means of digitization algorithms from Figure 1b reads (1300 ± 40) NP/μm^2. Knowing the total amount of material deposited (2.5 nm equivalent thickness), the mean NP volume is found just short of 2×10^3 nm^3, while the mean NP-array pitch along the surface direction either parallel or perpendicular to the LiF nanoridges reads approximately 25 nm.

The optical response of the samples was assessed *in situ* by transmission measurements in the 2.75−12 eV photon energy range, at the BEAR beamline at the Elettra synchrotron radiation source. The transmission spectra were acquired at room temperature, in normal incidence, with linearly polarized light. The degree of linear polarization was 0.89 at 7.9 eV and 0.86 at 10.3 eV. The polarization direction was aligned either parallel or perpendicular to the LiF ridge direction. We will refer to these geometries as longitudinal (*L*) or transverse (*T*), respectively. The optical transmission spectra were all measured within 1 h of the sample fabrication and have been normalized to the bare-LiF transmission spectrum. The LiF crystals used in this experiment were transparent up to an energy $E > 11.5$ eV, hence perfectly suited for DUV transmission experiments.

In Figure 1c,d, we report the optical-extinction spectra, measured on the *same* sample in the NW and NP case, respectively. In the NW case, the *L* excitation shows a broad, low-energy extinction, peaking in the visible regime. Conversely, the transverse extinction exhibits a narrower, blueshifted peak with its maximum at 6.6 eV and a broad DUV tail extending as far as 11 eV. The extinction spectra dramatically change after annealing. In the *L* geometry, the main extinction peak is now found at 5.6 eV, with a pronounced high-energy shoulder around 8.5 eV. In *T* geometry, instead, the main extinction peak is now found at 6.8 eV, with a prominent shoulder on its high-energy side at 8.5−9 eV that endows the resonance with a fairly broadband character all over the DUV range (fwhm ≈ 3.7 eV).

Oxidation was performed within the UHV vessel, by controlled exposure to research-grade oxygen gas. Even at extremely small exposure, oxidation had a significant effect on the extinction spectra. In Figure 2, we report various spectra acquired for increasing oxygen exposures of the Al NPs. Figure 2a shows the *T*-geometry extinction following the exposure to 100 langmuir (1 langmuir = 1×10^{-6} mbar × s) of research grade O_2. In Figure 2b,c, the *L* and *T* spectra after the exposure to 5000 langmuir are reported, respectively. Figure 2d,e display the *L* and *T* spectra obtained upon 5 min of exposure to atmosphere. In each panel, the corresponding pristine spectrum is reported as a red line, in order to highlight the effects of oxidation.

Upon the 100 langmuir exposure, a value for which we expect oxygen atoms to merely start absorbing on the NP surface,[28] the *T*-spectrum changes were manifested as a barely detectable decrease of the high-energy shoulder and increase of the low-energy tail. At 5000 langmuir, the main effect on the *L* spectra was a quasi-rigid redshift of the LSP peak, by roughly 0.3 eV. In the *T* case, a similar redshift is accompanied by a strong damping of the high-energy shoulder. Upon exposure to atmophere, the *L* peak further red-shifted to 5.0 eV, became narrower and completely lost, within experimental uncertainty, its high-energy shoulder. Under analogous conditions, the *T* main peak slightly red-shifted with respect to the 5000 langmuir case (LSP energy 6.1 eV), but exhibited a further quenching of its high-energy side, becoming significantly narrower than the pristine case.

A few qualitative considerations can already be made looking at the spectra of Figures 1 and 2. First, we notice that the energy of the main extinction peak (6.8 eV), safely ascribed to the excitation of a LSP resonance,[2] is by far the highest ever reported for optical excitation of metallic particles. Previous high values ranged indeed between 5.8 and 5.9 eV, both for Al core−shell metal/oxide particles.[2,19] Although the BEAR setup did not allow to directly assess the Al NP oxygen content, the considerably higher LSP energy observed here in comparison with the analogous oxidized case[2] and the strong sensitivity of the LSP to oxygen exposure (*cf.* Figure 2) strongly substantiate the claim of having fabricated virtually oxygen-free nanoparticles. On the basis of the known sticking coefficient of molecular oxygen on Al,[29] the overall exposure to background pressure in the UHV vessel between fabrication and measurement, and previous works on the subject,[1] the spurious oxide thickness on the NP surface can be estimated below 0.2 nm, for an overall NP purity larger than 95%. This is the first time that such NPs are successfully characterized by optical spectroscopy.

Deeper insights about the influence of the mutual EM interaction between the NPs, the origin of the high-energy shoulders, the system's birefringence and the oxidation dynamics can be achieved comparing the experimental spectra with appropriate computational models. The main issues involved in modeling the self-organized NP arrays are thoroughly discussed in ref 2. In brief, the AFM characterization yields with fair accuracy the NP areal density and the NP-array pitch, from which the mean NP volume of 2×10^3 nm^3 and the mean pitch along and across the ripples, equal

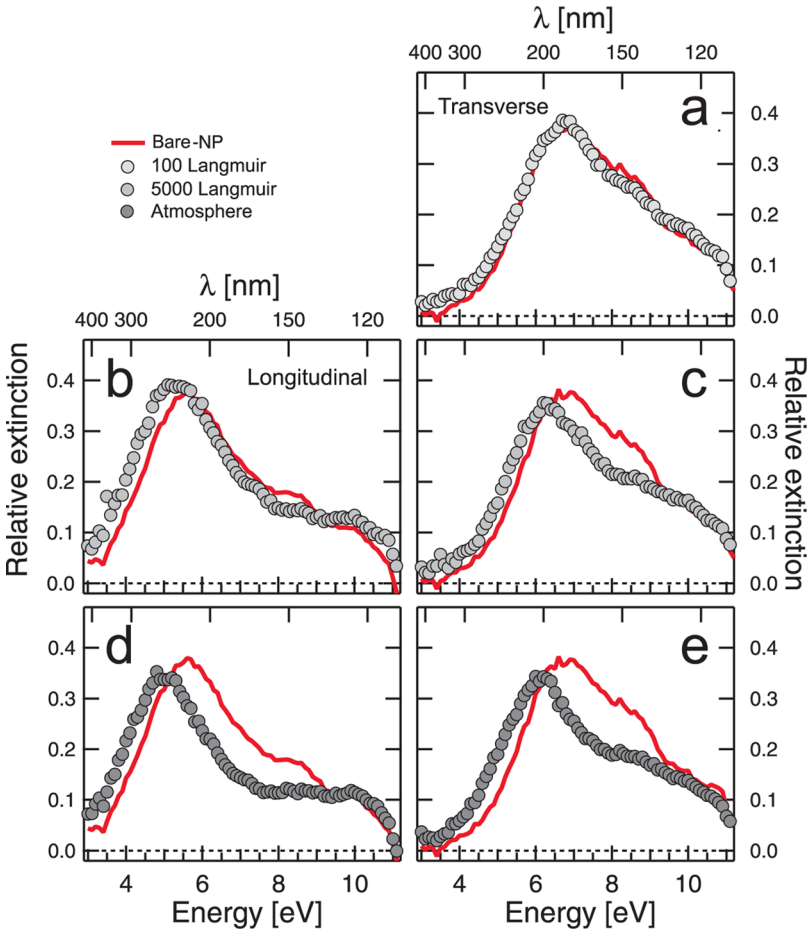

Figure 2. Plasmonic response *vs* oxidation. Extinction spectra of Al nanoparticles as a function of oxidation. (a, c, and e) Spectra measured in *T* geometry upon exposure to 100 langmuir, 5000 langmuir, and atmosphere (gray markers). (b and d) Spectra measured in *L* geometry upon exposure to 5000 langmuir and atmosphere (gray markers). In all panels, the extinction spectrum measured in the purely metallic case is reported as the red line.

to 25 nm, are deduced. The exact NP shape eludes the AFM analysis, while electron microscopies (in any case not available *in situ*) are strongly limited in their application by the heavily insulating nature of the substrate.

Thus, to proceed with the modeling, some basic hypothesis about the actual NP shape have to be made, which are gradually optimized by comparison with experimental data (see the Materials and Methods section for more details). We notice that the substantial absence of oxide effectively removes one morphological variable from the system modeling, allowing more freedom to explore the NP shape in simulations with respect to analogous oxidized cases.[2] The effect of the morphological array disorder (irregular array pitch, NP size dispersion) could not be realistically taken into account, due to computational-time/power limitations. Superradiant modes delocalized over several neighboring particles, like the low-energy dipolar modes, are however only weakly affected by array disorder effects.[30,31] Thus, neglecting shape/arrangement disorder in the simulations should impact more heavily the multipolar, high-energy part of the spectrum rather than the dipolar modes. When optimizing the particle geometry by experiment-theory comparison, we will accordingly mainly seek agreement in the dipolar part of the spectrum.

The best agreement between experimental and simulated extinction spectra is then found for the NP geometry and dimensions indicated in the top of Figure 3. The NP is partly laid on both the (010) and (100) facets. Such a configuration may physically originate from the tendency to maximize the exposed LiF surface, since its energy is considerably lower than the one of Al,[32,33] while the different contact angle with the (010) and (100) facet might be due to a residual hysteresis during the thermal NW dewetting. Other obvious geometries, such as assuming the NPs to be semiellipsoids laid on a single facet, yielded far too red-shifted values for both *L* and *T* geometries. We notice that the choice of a "smooth" NP shape, like an ellipsoid, neglects the likely presence of facets, edges and corners, that might contribute multipolar resonance modes.[34] However, probing many more geometries without independent input would add little to what can be learnt from the analysis of this model NP shape.

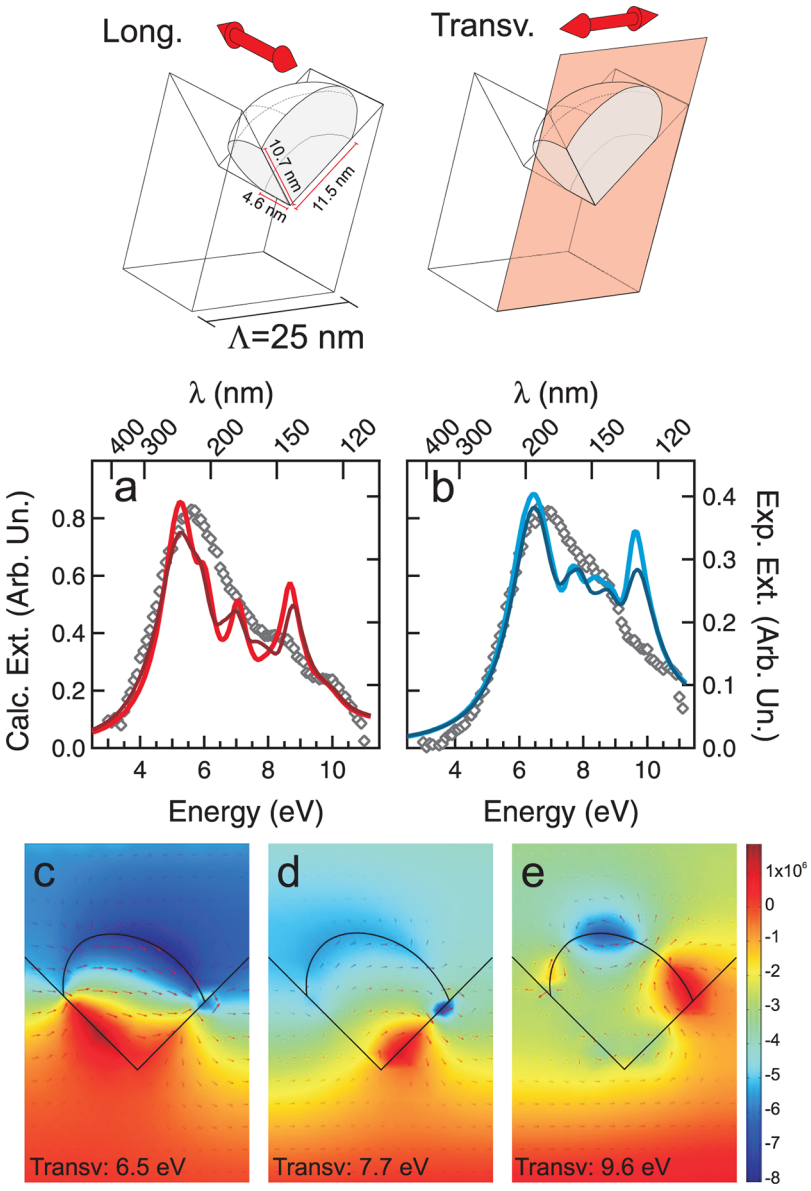

Figure 3. Simulations of the plasmonic response. (Top panel) NP geometry employed for simulations. (a and b) Calculated extinction spectra in (a) *L* and (b) *T* configuration for the Al NP geometry represented in the top panel (red, light-blue thick continuous lines) and for the incoherent summation of several spectra calculated applying perturbative changes to the NP shape (brown, blue thin continuous lines, see text for details). Markers show the experimental data. (c–e) Spatial maps of the magnetic-field component out of the image plane (color map) and of the electric currents (arrows) in *T* geometry at photon energies of (c) 6.5, (d) 7.7 and (e) 9.6 eV in the plane bisecting the NP and normal to the LiF ridges (top right panel).

The calculated *L* and *T* extinction spectra for the best-matching geometry are reported in Figure 3, panels a and b, respectively. The experimental spectra are reported as markers, for the sake of comparison. It immediately appears that, apart from a small red-shift that could not be accommodated by the simulations, the energy of the main extinction peaks is well reproduced, as is the large sample birefringence, clearly induced by the uniaxial system's symmetry. In the high-energy part, the calculations show multiple peaks: in *T* geometry, weak features are predicted in the 8–9 eV range, and a prominent peak is seen at 10 eV. In *L* geometry, almost-evenly spaced peaks appear at energies of roughly 6, 7, and 8.5 eV, respectively.

Quite generally, the high-energy features can be ascribed to the excitation of multipolar modes in the NPs. As an example, cross sections of the nanoparticle reporting the distribution of the (001) component (out of the image plane) of the magnetic field (color map) and the induced currents (arrows) are reported in Figure 3c–e for the *T* geometry, at energies of 6.5, 7.7, and 9.6 eV, respectively. The different number of nodes is clearly seen. Corresponding *L*-polarized maps are reported in the Supporting Information. Calculations performed for a *single* Al NP neglecting interparticle

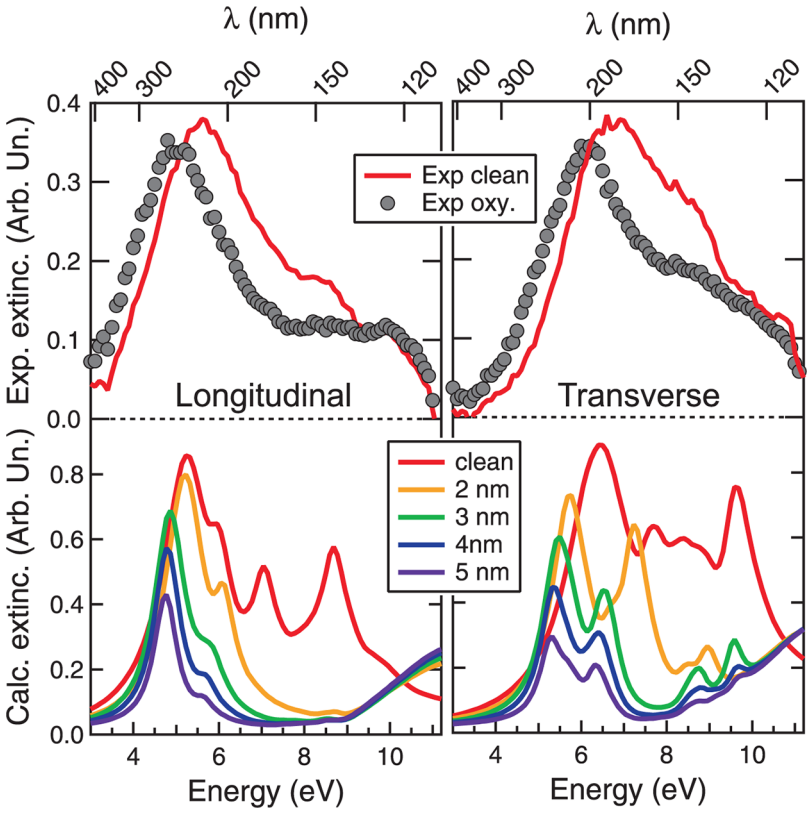

Figure 4. Experimental (top panels) and calculated (bottom panels) extinction spectra in *L* (left panels) and *T* (right panels) geometry as a function of oxidation. Experimental data: extinction spectra of pristine Al NPs (red line) and following a brief exposure to atmosphere (markers). Calculations: extinction spectra of the pristine NPs (red line), and in the presence of a homogeneous Al-oxide layer on the exposed NP surface, formed to the detriment of the Al metallic core (orange, 2 nm; green, 3 nm; blue, 4 nm; violet, 5 nm).

interactions are reported in the Supporting Information. There, we notice a strong damping of the high-energy part of the extinction with respect to the interacting-NP case. This suggests that most of the weight of the multipolar peaks is due to the effects of interparticle EM coupling in the array, rather than to single-particle characteristics. Concerning the electric-field enhancement ratio, the predicted values, sampled in *L* configuration at a distance of 0.5 nm from the NP surface within the interparticle gaps, read between 3 and 9 in the 5−10 eV energy range (see the Supporting Information).

The agreement between theory and experiment in the high-energy region is indeed worse than that for the main dipolar peak. Qualitatively, the main reason for this significant discrepancy is the poor modeling of size/shape/pitch disorder in the arrays.[2,30] To quantitatively support this statement, sets of simulations were performed as a function of perturbative changes of the NP shape, leaving however periodic boundary conditions unchanged. More details can be found in the Supporting Information. The high-energy region of these sets of spectra showed indeed much larger relative variations in peak height *and* energy than the corresponding low-energy, dipolar peak. Thus, the incoherent summation of a large number of extinction spectra obtained upon perturbative changes of the system's morphological parameters shows the tendency for sharp high-energy peaks to smoothen more effectively than dipolar peaks. Examples of the incoherent summation of a few spectra calculated upon a slight compression or expansion of the "model" ellipsoid along directions normal to the two LiF facets are reported in Figure 3a,b as the thin brown (blue) lines (see the Supporting Information). The slight smoothening of the high-energy peaks indicates that size/shape dispersion plays a role in the high-energy discrepancy. We expect analogous effects for the array-pitch/geometrical-arrangement dispersion.

Turning our attention to the effect of oxidation, we report in Figure 4 the extinction spectra calculated in *L* and *T* geometry, respectively, in the presence of a homogeneous oxide shell on the exposed NP surface created to the detriment of the core itself, keeping the different Al-atom density in the metal and oxide into account. The calculated oxidized spectra are reported in the bottom panels, for a different thickness of the oxide layer, from 2 to 5 nm (the experimental spectra of pristine NPs and NPs exposed to atmosphere are reported in the top graphs, for the sake of comparison). An overall damping of the high-energy part of the extinction spectra is witnessed in both optical

geometries, in general agreement with the experimental data. This can be ascribed to a simultaneous shrinking of the metal cores and increase in their mutual distance, both effects leading to a damping of the multipolar contributions.

In *T* geometry, the experimental dipolar-peak redshift upon oxidation is already correctly reproduced for only 2 nm of oxide, while, interestingly, the redshift in *L* geometry approaches the experimental value only when the oxide thickness is modeled as 5 nm thick. With all the necessary care about the correctness of the NP shape, the difference between the experimental and calculated oxidation trends suggests that the simple picture of homogeneous oxide formation on the exposed NP surface might not catch the full physics of the oxidation process.

The fact that NPs exhibit a different oxidation dynamics with respect to flat surfaces, due to the high curvature of the NP surface and the presence of reactive sites, is by now well established.[24,35−38] Interestingly, however, deviations from perfectly spherical shape of the pristine metallic NPs (due to edges, corners or the contact with the substrate) produce a shape modification of the metallic core during oxidation.[39,40] Low-coordinated surface sites (edges, corners) can indeed act as preferential absorption sites, and gradually turn a faceted particle into a more spherical one, or produce less-conventional metal-core shapes[39] or vacancy clusters[40] that yield an evolution of the plasmonic response not accounted for by the homogeneous-oxide model.

CONCLUSIONS

Summarizing, we reported the plasmonic response of oxide-free Al nanoparticles, arranged in densely packed two-dimensional arrays on the surface of insulating LiF crystals. The NPs exhibit a broadband plasmonic response in the deep-ultraviolet region of the EM spectrum, peaking at an energy of 6.8 eV ($\lambda \approx 180$ nm), by far the highest ever reported for a LSP resonance observed by optical excitation of metallic nanoparticles. The dense packing of the NP in the arrays induces a multitude of DUV-active hot spots, with a density above $10^{11}/cm^2$, having estimated field-enhancement ratios up to almost 10 in the DUV range within the interparticle gaps. Comparison with theoretical models allowed to ascribe the broadband DUV plasmonic features to the excitation of dipolar and high-order collective plasmon modes, and suggested a possible shape evolution of the NP with ongoing oxidation.

Such DUV plasmon represents the current overall high-energy limit for LSP resonances and, so far, the only experimental counterpart of the various theoretical estimations of plasmonic activity of pure Al in the DUV. The combination of small NP size and dense NP packing achieved in our 2D arrays simultaneously yields DUV LSP resonances and a very broadband excitation that is partly preserved upon a quick exposure to atmosphere.

At the present state of technology, applications of purely metallic Al NPs may seem scarce due to the complex fabrication and, most notably, to the environmental influence on their plasmonic response. Future developments, both in science and technology, might however circumvent current limitations; graphene coating, successfully applied for the environmental shielding of Ag NPs, could be just one such possibility.[41] Though challenging in fabrication, atmosphere-resistant, DUV-plasmon-active substrates may become a reality, and represent an advantage in dedicated experiments featuring DUV EM excitation for Raman experiments,[17,42] label-free detection of biomolecules,[43,44] high-resolution microscopy[45] and nanolithography,[46] taking plasmonics toward spectral ranges where molecular resonances, materials' response and physical-process cross sections can be significantly different with respect to the visible-IR spectral window.

MATERIALS AND METHODS

Fabrication. The samples were fabricated by means of bottom-up procedures that easily lend themselves to be applied under UHV conditions, allowing to fabricate extremely small metallic nanoparticles.[2,26,27] Morphologically flat LiF(110) substrates were purchased from Crystec Gmbh. Nanopatterned LiF(110) surfaces, featuring a ridge-valley surface morphology, consisting of evenly spaced [100] and [010] facets separated by macrosteps, with a periodicity $\Lambda \approx 25$ nm (Figure 1, top) were fabricated by homoepitaxial deposition of ≈240 nm of LiF at 570 K.[26,27,47] Following an *ex situ* atomic-force microscopy (AFM) characterization (Multimode/Nanoscope IV system, Digital Instruments-Veeco, tapping mode), the nanopatterned substrates were transported to the BEAR beamline endstation at the Elettra synchrotron radiation source, and loaded in its preparation chamber.[48−50] Al films with equivalent thickness (defined as the equivalent thickness of material needed to achieve a uniform substrate coverage) of 2.5 nm were then deposited at room temperature (RT) by molecular-beam epitaxy at grazing incidence (60° from the normal) on the nanopatterned LiF(110) (Al 99.999% purity, Alfa Aesar) in the preparation chamber of BEAR. The Al thickness was determined by a calibrated quartz-crystal monitor. Thanks to the shadow effect of the nanoridges, elongated metallic structures were formed along the LiF ridges (nanowires, NW). The system was then flashed at 670 K in vacuum for 5 min to promote the dewetting of the Al NWs and the corresponding formation of arrays of disconnected NPs.[2,27] The preparation chamber at BEAR is connected with the measurements chamber under UHV conditions, so that the samples are not exposed to atmosphere between fabrication and measurement. The base pressure in the BEAR chamber is in the 10^{-10} mbar range, and never exceeded 3×10^{-9} mbar during the sample preparation.

Calculations. The simulations were performed employing a commercial FEM software, COMSOL Multiphysics. The array was modeled by designing a unit cell with periodic boundary conditions on the lateral sides. Extinction spectra were calculated directly from the transmission data collected by means of

a port analysis at different energies, from 2.5 to 11.5 eV. Perfectly matched layers have been placed beyond the ports to avoid unphysical reflections at the boundaries of the simulation domain. Aluminum, aluminum oxide and LiF dispersive optical parameters have been taken from refs 51, 52, and 53, respectively. Geometry discretization has been accomplished by meshing the cell with tetrahedral elements with a maximum element size to allow convergence of the results. For the NP shape, we started, after ref 2, by assuming an oblate ellipsoid, laid on the (010) facet of the LiF nanopatterns, having its "out-of-plane" semiaxis (normal to the (010) facet) equal to 0.7 times the in-plane semiaxis, and truncated at the intersection with the (010) and (100) facet planes. The extinction spectra were optimized as a function of rigid shifts of such ellipsoid with respect to the LiF nanogroove, keeping the array pitch unchanged, truncating the NP at the intersection with the facets and rescaling the NP dimensions in correspondence of each truncation in order to maintain the ellipsoid volume at the experimental value of 2×10^3 nm^3.

Conflict of Interest: The authors declare no competing financial interest.

Acknowledgment. The authors acknowledge Marco Lazzarino and the biophysics group at the Università di Genova for access to the AFM equipment, and Ennio Vigo for technical assistance. Partial support from Sincrotrone Elettra S.C.p.A. (PIK Ex.Pro.Rel.), the University of Genova (PRA 2012, PRA 2013) and the Ministero dell'Istruzione, dell'Università e della Ricerca (PRIN 20105ZZTSE_003) is acknowledged. The image analysis was performed using the open-source software Gwyddion.[54]

Supporting Information Available: Spatial maps of magnetic fields and currents calculated in longitudinal geometry, extinction-efficiency spectra calculated for Al NPs neglecting the interparticle EM interactions, electric-field enhancement factor *vs* photon energy and sets of extinction spectra calculated for perturbative variations of the NP shape. This material is available free of charge *via* the Internet at http://pubs.acs.org.

REFERENCES AND NOTES

1. Knight, M. W.; King, N. S.; Liu, L.; Everitt, H. O.; Nordlander, P.; Halas, N. J. Aluminum for Plasmonics. *ACS Nano* **2014**, *8*, 834–840.
2. Maidecchi, G.; Gonella, G.; Proietti Zaccaria, R.; Moroni, R.; Anghinolfi, L.; Giglia, A.; Nannarone, S.; Mattera, L.; Dai, H.-L.; Canepa, M.; *et al.* Deep Ultraviolet Plasmon Resonance in Aluminum Nanoparticle Arrays. *ACS Nano* **2013**, *7*, 5834–5841.
3. Langhammer, C.; Schwind, M.; Kasemo, B.; Zorić, I. Localized Surface Plasmon Resonances in Aluminum Nanodisks. *Nano Lett.* **2008**, *8*, 1461–1471.
4. Ekinci, Y.; Solak, H. H.; Löffler, J. F. Plasmon Resonances of Aluminum Nanoparticles and Nanorods. *J. Appl. Phys.* **2008**, *104*, 083107.
5. Zorić, I.; Zäch, M.; Kasemo, B.; Langhammer, C. Gold, Platinum, and Aluminum Nanodisk Plasmons: Material Independence, Subradiance, and Damping Mechanisms. *ACS Nano* **2011**, *5*, 2535–2546.
6. Castro-Lopez, M.; Brinks, D.; Sapienza, R.; van Hulst, N. F. Aluminum for Nonlinear Plasmonics: Resonance-Driven Polarized Luminescence of Al, Ag, and Au Nanoantennas. *Nano Lett.* **2011**, *11*, 4674–4678.
7. Chan, G. H.; Zhao, J.; Schatz, G. C.; Duyne, R. P. V. Localized Surface Plasmon Resonance Spectroscopy of Triangular Aluminum Nanoparticles. *J. Phys. Chem. C* **2008**, *112*, 13958–13963.
8. Zeman, E. J.; Schatz, G. C. An Accurate Electromagnetic Theory Study of Surface Enhancement Factors for Silver, Gold, Copper, Lithium, Sodium, Aluminum, Gallium, Indium, Zinc, and Cadmium. *J. Phys. Chem.* **1987**, *91*, 634–648.
9. Hu, J.; Chen, L.; Lian, Z.; Cao, M.; Li, H.; Sun, W.; Tong, N.; Zeng, H. Deep-Ultraviolet-Blue-Light Surface Plasmon Resonance of Al and Al_{core}/Al_2O_{3shell} in Spherical and Cylindrical Nanostructures. *J. Phys. Chem. C* **2012**, *116*, 15584–15590.
10. Hornyak, G. L.; Phani, K. L. N.; Kunkel, D. L.; Menon, V. P.; Martin, C. R. Fabrication, Characterization and Optical Theory of Aluminum Nanometal/Nanoporous Membrane Thin Film Composites. *Nanostruct. Mater.* **1995**, *6*, 839–842.
11. Jiao, X.; Blair, S. Polarization Multiplexed Optical Bullseye Antennas. *Plasmonics* **2012**, *7*, 39–46.
12. Jeyaram, Y.; Jha, S. K.; Agio, M.; Löffler, J. F.; Ekinci, Y. Magnetic Metamaterials in the Blue Range Using Aluminum Nanostructures. *Opt. Lett.* **2010**, *35*, 1656–1658.
13. Taguchi, A.; Saito, Y.; Watanabe, K.; Yijian, S.; Kawata, S. Tailoring Plasmon Resonances in the Deep-Ultraviolet by Size-Tunable Fabrication of Aluminum Nanostructures. *Appl. Phys. Lett.* **2012**, *101*, 081110.
14. Knight, M. W.; Liu, L.; Wang, Y.; Brown, L.; Mukherjee, S.; King, N. S.; Everitt, H. O.; Nordlander, P.; Halas, N. J. Aluminum Plasmonic Nanoantennas. *Nano Lett.* **2012**, *12*, 6000–6004.
15. Ferry, V. E.; Polman, A.; Atwater, H. A. Modeling Light Trapping in Nanostructured Solar Cells. *ACS Nano* **2011**, *5*, 10055–10064.
16. Akimov, Y.; Koh, W. Design of Plasmonic Nanoparticles for Efficient Subwavelength Light Trapping in Thin-Film Solar Cells. *Plasmonics* **2011**, *6*, 155–161.
17. Jha, S. K.; Ahmed, Z.; Agio, M.; Ekinci, Y.; Löffler, J. F. Deep-UV Surface-Enhanced Resonance Raman Scattering of Adenine on Aluminum Nanoparticle Arrays. *J. Am. Chem. Soc.* **2012**, *134*, 1966–1969.
18. Taguchi, A.; Hayazawa, N.; Furusawa, K.; Ishitobi, H.; Kawata, S. Deep-UV Tip-Enhanced Raman Scattering. *J. Raman Spectrosc.* **2009**, *40*, 1324–1330.
19. Martin, J.; Proust, J.; Gérard, D.; Plain, J. Localized Surface Plasmon Resonances in the Ultraviolet from Large Scale Nanostructured Aluminum Films. *Opt. Mater. Express* **2013**, *3*, 954–959.
20. Moscatelli, A. Plasmonics: the Aluminum Rush. *Nat. Nanotechnol.* **2012**, *7*, 778.
21. Chen, Q.; Das, D.; Chitnis, D.; Walls, K.; Drysdale, T.; Collins, S.; Cumming, D. A CMOS Image Sensor Integrated with Plasmonic Colour Filters. *Plasmonics* **2012**, *7*, 695–699.
22. Blaber, M. G.; Arnold, M. D.; Ford, M. J. Search for the Ideal Plasmonic Nanoshell: The Effects of Surface Scattering and Alternatives to Gold and Silver. *J. Phys. Chem. C* **2009**, *113*, 3041–3045.
23. Sanz, J. M.; Ortiz, D.; Alcaraz de la Osa, R.; Saiz, J. M.; González, F.; Brown, A. S.; Losurdo, M.; Everitt, H. O.; Moreno, F. UV Plasmonic Behavior of Various Metal Nanoparticles in the Near- and Far-Field Regimes: Geometry and Substrate Effects. *J.Phys. Chem. C* **2013**, *117*, 19606–19615.
24. Cabrera, N.; Mott, N. F. Theory of the Oxidation of Metals. *Rep. Prog. Phys.* **1948**, *12*, 163–184.
25. Ross, M. B.; Schatz, G. C. Aluminum and Indium Plasmonic Nanoantennas in the Ultraviolet. *J. Phys. Chem. C* **2014**, *118*, 12506–12514.
26. Kitahara, T.; Sugawara, A.; Sano, H.; Mizutani, G. Optical Second-Harmonic Spectroscopy of Au Nanowires. *J. Appl. Phys.* **2004**, *95*, 5002–5005.
27. Anghinolfi, L.; Moroni, R.; Mattera, L.; Canepa, M.; Bisio, F. Flexible Tuning of Shape and Arrangement of Au Nanoparticles in 2-Dimensional Self-Organized Arrays: Morphology and Plasmonic Response. *J. Phys. Chem. C* **2011**, *115*, 14036–14043.
28. Berg, C.; Raaen, S.; Borg, A.; Andersen, J. N.; Lundgren, E.; Nyholm, R. Observation of a Low-Binding-Energy Peak in the 2 *p* Core-Level Photoemission from Oxidized Al(111). *Phys. Rev. B* **1993**, *47*, 13063–13066.
29. Popova, I.; Zhukov, V.; Y, J., Jr Comparative Study of Al(111) Oxidation with O_3 and O_2. *Surf. Sci.* **2002**, *518*, 39–48.
30. Slaughter, L. S.; Willingham, B. A.; Chang, W.-S.; Chester, M. H.; Ogden, N.; Link, S. Toward Plasmonic Polymers. *Nano Lett.* **2012**, *12*, 3967–3972.

31. Halas, N. J.; Lal, S.; Chang, W.-S.; Link, S.; Nordlander, P. Plasmons in Strongly Coupled Metallic Nanostructures. *Chem. Rev.* **2011**, *111*, 3913–3961.
32. Gilman, J. J. Direct Measurements of the Surface Energies of Crystals. *J. Appl. Phys.* **1960**, *31*, 2208–2218.
33. Vitos, L.; Ruban, A.; Skriver, H. L.; Kollár, J. The Surface Energy of Metals. *Surf. Sci.* **1998**, *411*, 186–202.
34. Noguez, C. Surface Plasmons on Metal Nanoparticles: The Influence of Shape and Physical Environment. *J. Phys. Chem. C* **2007**, *111*, 3806–3819.
35. Sutter, E.; Sutter, P. Size-Dependent Room Temperature Oxidation of In Nanoparticles. *J. Phys. Chem. C* **2012**, *116*, 20574–20578.
36. Ermoline, A.; Dreizin, E. L. Equations for the Cabrera–Mott Kinetics of Oxidation for Spherical Nanoparticles. *Chem. Phys. Lett.* **2011**, *505*, 47–50.
37. Zhdanov, V. P.; Kasemo, B. Cabrera–Mott Kinetics of Oxidation of nm-Sized Metal Particles. *Chem. Phys. Lett.* **2008**, *452*, 285–288.
38. Park, K.; Lee, D.; Rai, A.; Mukherjee, D.; Zachariah, M. R. Size-Resolved Kinetic Measurements of Aluminum Nanoparticle Oxidation with Single Particle Mass Spectrometry. *J. Phys. Chem. B* **2005**, *109*, 7290–7299.
39. Pratt, A.; Lari, L.; Hovorka, O.; Shah, A.; Woffinden, C.; Tear, S. P.; Binns, C.; Kröger, R. Enhanced Oxidation of Nanoparticles through Strain-Mediated Ionic Transport. *Nat. Mater.* **2014**, *13*, 26–30.
40. Nakamura, R.; Tokozakura, D.; Nakajima, H.; Lee, J.-G.; Mori, H. Hollow Oxide Formation by Oxidation of Al and Cu Nanoparticles. *J. Appl. Phys.* **2007**, *101*, 074303.
41. Reed, J. C.; Zhu, H.; Zhu, A. Y.; Li, C.; Cubukcu, E. Graphene-Enabled Silver Nanoantenna Sensors. *Nano Lett.* **2012**, *12*, 4090–4094.
42. Kumamoto, Y.; Taguchi, A.; Smith, N. I.; Kawata, S. Deep UV Resonant Raman Spectroscopy for Photodamage Characterization in Cells. *Biomed. Opt. Expr.* **2011**, *2*, 927–936.
43. Anker, J. N.; Hall, W. P.; Lyandres, O.; Shah, N. C.; Zhao, J.; Van Duyne, R. P. Biosensing with Plasmonic Nanosensors. *Nat. Mater.* **2008**, *7*, 442–453.
44. Kabashin, A. V.; Evans, P.; Pastkovsky, S.; Hendren, W.; Wurtz, G. A.; Atkinson, R.; Pollard, R.; Podolskiy, V. A.; Zayats, A. V. Plasmonic Nanorod Metamaterials for Biosensing. *Nat. Mater.* **2009**, *8*, 867–871.
45. Gramotnev, D. K.; Bozhevolnyi, S. I. Plasmonics beyond the Diffraction Limit. *Nat. Photonics* **2010**, *4*, 83–91.
46. Totzeck, M.; Ulrich, W.; Gohnermeier, A.; Kaiser, W. Semiconductor Fabrication: Pushing Deep Ultraviolet Lithography to Its Limits. *Nat. Photonics* **2007**, *1*, 629–631.
47. Sugawara, A.; Mae, K. Surface Morphology of Epitaxial LiF(110) and CaF_2(110) Layers. *J. Vac. Sci. Technol., B* **2005**, *23*, 443–448.
48. Naletto, G.; Pelizzo, M. G.; Tondello, G.; Nannarone, S.; Giglia, A. Monochromator for the Synchrotron Radiation Beamline X-MOSS at ELETTRA. *Proc. SPIE* **2001**, *4145*, 105–113.
49. Nannarone, S.; Giglia, A.; Mahne, N.; DeLuisa, B. A.; Doyle; Borgatti, F.; Pedio, M.; Pasquali, L.; Naletto, G.; Pelizzo, M. G.; Tondello, G. BEAR: A Bending Magnet for Emission, Absorption and Reflectivity. *Neutroni Luce Sincrotrone* **2007**, *12*, 8–19.
50. Nannarone, S.; Borgatti, F.; DeLuisa, A.; Doyle, B. P.; Gazzadi, G. C.; Giglia, A.; Finetti, P.; Mahne, N.; Pasquali, L.; Pedio, M.; *et al.* The BEAR Beamline at Elettra. *AIP Conf. Proc.* **2004**, *705*, 450–453.
51. Rakic, A. D.; Djurišic, A. B.; Elazar, J. M.; Majewski, M. L. Optical Properties of Metallic Films for Vertical-Cavity Optoelectronic Devices. *Appl. Opt.* **1998**, *37*, 5271–5283.
52. Palik, E. D., Ed. *Handbook of Optical Constants of Solids*; Academic Press: New York, 1985.
53. Li, H. H. Refractive Index of Alkali Halides and Its Wavelength and Temperature Derivatives. *J. Phys. Chem. Ref. Data* **1976**, *5*, 329–528.
54. Necas, D.; Klapetek, P. Gwyddion: An Open-Source Software for SPM Data Analysis. *Cent. Eur. J. Phys.* **2012**, *10*, 181–188.